Sensitivity of Simulated Global Climate to Perturbations in Low-Cloud Microphysical Properties. Part I: Globally Uniform Perturbations

C.-T. CHEN* AND V. RAMASWAMY

Atmospheric and Oceanic Sciences Program, Princeton University, Princeton, New Jersey

(Manuscript received 21 June 1995, in final form 20 November 1995)

ABSTRACT

The sensitivity of the global climate to perturbations in the microphysical properties of low clouds is investigated using a general circulation model coupled to a static mixed layer ocean with fixed cloud distributions and incorporating a new broadband parameterization for cloud radiative properties. A series of GCM experiments involving globally uniform perturbations in cloud liquid water path or effective radius (albedo perturbations), along with one for a doubling of carbon dioxide (greenhouse perturbation), lead to the following results: 1) The model's climate sensitivity (ratio of global-mean surface temperature response to the global-mean radiative forcing) is virtually independent (to ~10%) of the sign, magnitude, and the spatial pattern of the forcings considered, thus revealing a linear and invariant nature of the model's global-mean response. 2) Although the total climate feedback is very similar in all the experiments, the strengths of the individual feedback mechanisms (e.g., water vapor, albedo) are different for positive and negative forcings. 3) Changes in moisture, tropospheric static stability, and sea ice extent govern the vertical and zonal patterns of the temperature response, with the spatial distribution of the response being quite different from that of the radiative forcing. 4) The zonal surface temperature response pattern, normalized with respect to the global mean, is different for experiments with positive and negative forcings, particularly in the polar regions of both hemispheres, due to differing changes in sea ice. 5) The change in the surface radiative fluxes is different for the carbon dioxide doubling and cloud liquid water path decrease experiments, even though both cases have the same radiative forcing and a similar global-mean surface temperature response; this leads to differences in the vigor of the hydrologic cycle (evaporation and precipitation rates) in these two experiments.

1. Introduction

From theoretical, modeling, and observational studies on cloud microphysical properties and their relationships with the environment (Feigelson 1978; Charlson et al. 1987; Betts and Harshvardhan 1987; Tselioudis et al. 1992; Han et al. 1994), it may be summarized that cloud microphysical properties [e.g., liquid water path (LWP) and drop effective radius r_e] are critical factors in determining the radiative properties of clouds. General circulation models indicate a critical dependence of climate on cloud properties (e.g., Wetherald and Manabe 1988, hereafter WM; Roeckner et al. 1987). Furthermore, variations in cloud microphysics due to natural or anthropogenic influences (Twomey et al. 1984; Somerville and Remer 1984; Coakley et al. 1987; Radke et al. 1989; Charlson et al. 1992) imply a change in their radiative properties, which in turn has implications for climate change. It is the potential climatic significance of the variations in cloud microphysical properties, as framed by the above studies, that motivates this sensitivity study.

Our main objective in this paper is to inquire into the climate sensitivity to perturbations in cloud microphysics, which, in a more general sense, imply perturbations in the albedo of the earth's climate system. As specific foci for the study, we pose the following issues: (i) whether the climate response to a change in cloud microphysical and, thus, radiative properties scales linearly with the strength of the radiative forcing; (ii) whether the magnitude of the response is similar when forcings of equal strength but with opposite signs are applied; (iii) whether changes in LWP or r_e that yield the same change in cloud optical depth lead to a similar response; and (iv) whether the responses to a change in cloud radiative properties and that due to increase of CO_2 are of a similar nature.

We pursue an investigation of the above issues by conducting an idealized general circulation model investigation of the sensitivity of the simulated climate to globally uniform percentage changes in the LWP or r_e of low clouds. There are two reasons for adopting

* Current affiliation: National Taiwan Normal University, Taipei, Taiwan.

Corresponding author address: Dr. V. Ramaswamy, Atmospheric and Oceanic Science Program, NOAA/Geophysical Fluid Dynamics Laboratory, Princeton University, P.O. Box 308, Princeton, NJ 08542.
E-mail: vr@gfdl.gov

the strategy of idealized experiments. First, although there is evidence suggesting possible modifications in cloud microphysics, the spatial and temporal quantification of such effects are not yet robust. Second, a suite of idealized experiments, as discussed in this paper, is useful for yielding insights into the characteristics of the responses to changes in cloud microphysics and offers ease and simplicity in interpreting the physical changes.

The numerical values of the changes in LWP and r_e chosen for the different GCM experiments are such that they yield global-mean forcings ranging up to ~4 W m^{-2}, which corresponds to that due to a doubling of CO_2. We restrict the perturbation of the cloud microphysical properties in this study to low-level clouds only. These clouds are a major component of the global cloud cover (Warren et al. 1988) and play a significant role in the radiative balance of the planet (Hartmann et al. 1992). The low-cloud microphysics are likely subject to a modification, owing to surface-based marine or anthropogenic sources of CCN (Hoppel et al. 1973).

In order to further simplify the scope of this GCM study, we consider the changes in the cloud microphysical properties to be an external forcing. Other cloud properties, such as amount and distribution, are prescribed and held fixed during the simulation experiments. Thus, only the noncloud feedback processes participate in response to the imposed forcing. Since low clouds have large LWPs such that their longwave emissivities are close to unity, any perturbation in the microphysics is expected to alter the cloud longwave radiation properties negligibly; it is, therefore, not a factor in this study.

We first discuss the model and describe the simulation of a new control climate in which the solar cloud properties are computed based on prescribed LWP and r_e values (section 2). Then, the GCM sensitivity experiments consisting of globally uniform prescribed changes in cloud LWP or r_e are discussed, along with the characteristics of the accompanying forcings. The response of the modeled climate to the imposed perturbations is investigated in section 3. This includes the spatial distribution of the changes in the thermal and hydrologic fields and the manner in which the surface energy budget in the various experiments is altered. The individual feedback processes operating in the present model framework and their relative importance, as well as the role of the feedbacks in the different experiments, are analyzed in section 4. The implications of the findings are discussed in section 5.

2. Model and formulation of the GCM experiments

a. Description of the model

The climate model used for the following study is an R15, 9-level global atmospheric GCM coupled to a static mixed layer ocean. The process of sea ice formation is explicitly incorporated into the model, but the effect of heat transport by ocean currents is not included. The seasonal cycle of insolation is prescribed at the top of the atmosphere, but diurnal variation is ignored. Seasonally invariant, zonally uniform cloud cover is prescribed with respect to latitude and height.

The model is essentially the same as the fixed cloud (FC) version used by Manabe and Broccoli (1985, hereafter MB), with the following exceptions: (i) the cloud solar radiative properties are determined using Slingo's (1989) parameterization, (ii) the broadband solar radiative transfer algorithm is modified to account for the details of the vapor–drop interactions (Chen and Ramaswamy 1995, hereafter CR), and (iii) the albedo value assigned to snow and sea ice is modified slightly following Manabe et al. (1991) (i.e., the albedo of snow/ice depends on the surface temperature and snow/ice thickness; the albedo values are saturated at a thickness of 1 meter). Since we have changed the cloud radiative and surface albedo parameterizations in the model, the simulated control climate differs from that reported in MB. The cloud LWP and r_e for each of the three cloud layers are assigned uniform values all over the globe, with the zonal cloud amounts being the same as in MB.

For simplicity, the drop effective radius r_e is assumed to be 10 μm for all clouds. Most clouds in the lower troposphere exhibit a droplet mode radius between 5 and 15 μm (Mason 1971; Stephens 1979). This assumption has been used to infer cloud optical thickness from satellite-based visible radiances (Rossow and Schiffer 1991) and is likely uncertain by 15%–25% for water clouds (Rossow et al. 1989; Nakajima and King 1990; Han et al. 1994). The assumed r_e value may not be entirely appropriate for high clouds containing ice crystals having larger dimensions and/or nonspherical shapes. However, the high-cloud characteristics are not the focus of the present study. The LWP of high and middle clouds is fixed at 7 and 25 g m^{-2}, respectively, while the nominal value assigned to the low clouds is 80 g m^{-2}. For low clouds, the choice of LWP and r_e yields an optical depth of 12.7 at visible wavelengths, approximately consistent with satellite observations (Rossow and Lacis 1990) and aircraft measurements in marine stratus clouds (Nakajima et al. 1991). Satellite-derived estimates over the global oceans (Greenwald et al. 1993) suggest that the zonal-mean cloud LWPs range from 50 to 150 g m^{-2}, with a relative error of 25% to 40%. Our choice of LWPs lies within the range cited. The LWP values chosen are such that net solar radiative flux at the top of the atmosphere (TOA) is within about 10 W m^{-2} of satellite measurements (Chen 1994).

b. Standard ("control") simulation

The control climate of the model is the average of the last 10 years results from a 40-year integration with

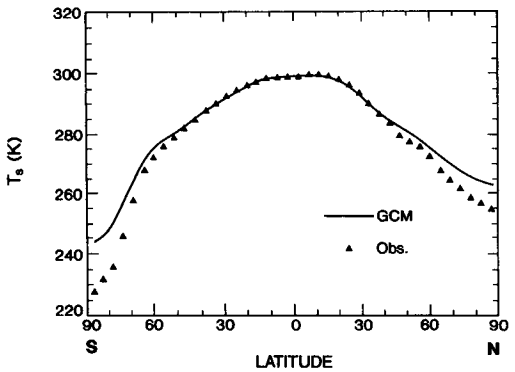

FIG. 1. Zonal annual-mean surface air temperature in the simulated "control" climate.

the modifications noted above. Figure 1 shows the latitudinal distribution of the simulated zonal-mean surface air temperature along with the observed values [from Crutcher and Meserve (1970) and Taljaard et al. (1969)]. In general, the simulated surface temperatures are quite close to the observed values throughout the tropical and midlatitude regions in both hemispheres. Poleward of 55°, the model temperatures are somewhat too warm, particularly in the Antarctic. Compared to the control simulation in MB, the present result yields a warmer climate in the Arctic region. This is because the cloud reflectivity obtained from the new cloud radiative parameterization is slightly smaller than that prescribed in MB, especially at the high latitudes where the solar zenith angle is large. The amplitude and phase of the seasonal variation of surface air temperature are reasonably well simulated (Chen 1994), although the amplitude of the computed seasonal variation is somewhat smaller than that observed near the poles (especially the North Pole).

Figure 2a shows the simulated sea ice distribution in the Northern Hemisphere during winter (Dec, Jan, Feb). Comparing with the observed maximum sea ice extent during the same season [Fig. 2b; Untersteiner (1984), reproduced from Peixoto and Oort (1992)], it is seen that the computed sea ice margin is located slightly more poleward than observed during winter, in association with the warmer (relative to observed) simulated temperatures (Fig. 1). In the Southern Hemisphere (Fig. 3), the model underestimates the areal coverage of the sea ice during winter (Jun, Jul, Aug). Overall, the spatial pattern simulated by the model shows modest agreement with observations in both polar regions.

Figure 4 illustrates the latitudinal profile of the modeled and observed (Baumgartner and Reichel 1975) zonal-mean precipitation and evaporation rates. The model succeeds in reproducing the extensive rainfall in the Tropics. However, the precipitation rate in the present low-resolution spectral model simulation is overestimated at the high latitudes (see also Manabe et al. 1979; Manabe and Stouffer 1980, hereafter MS). Zonal-mean evaporation rates are simulated better than the precipitation rates (Fig. 4b), with discrepancies near 10°N and poleward of 60°.

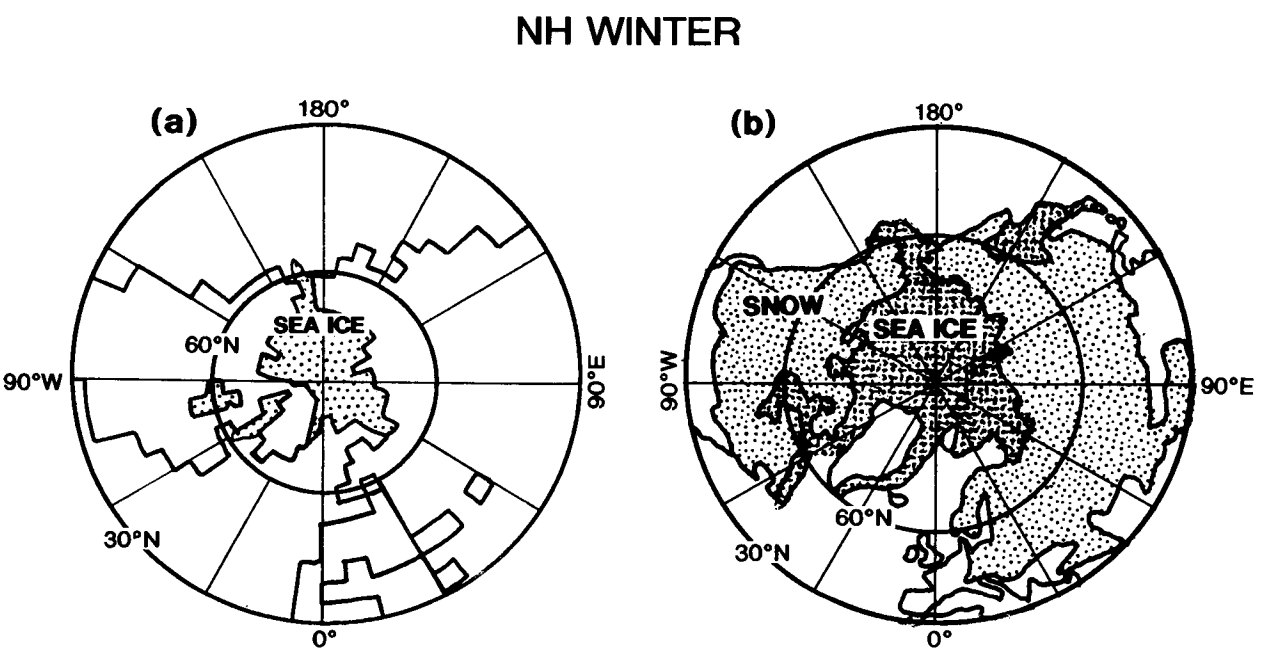

FIG. 2. Geographical distribution of sea ice during the Northern Hemisphere winter: (a) control simulation and (b) observation (Untersteiner 1984).

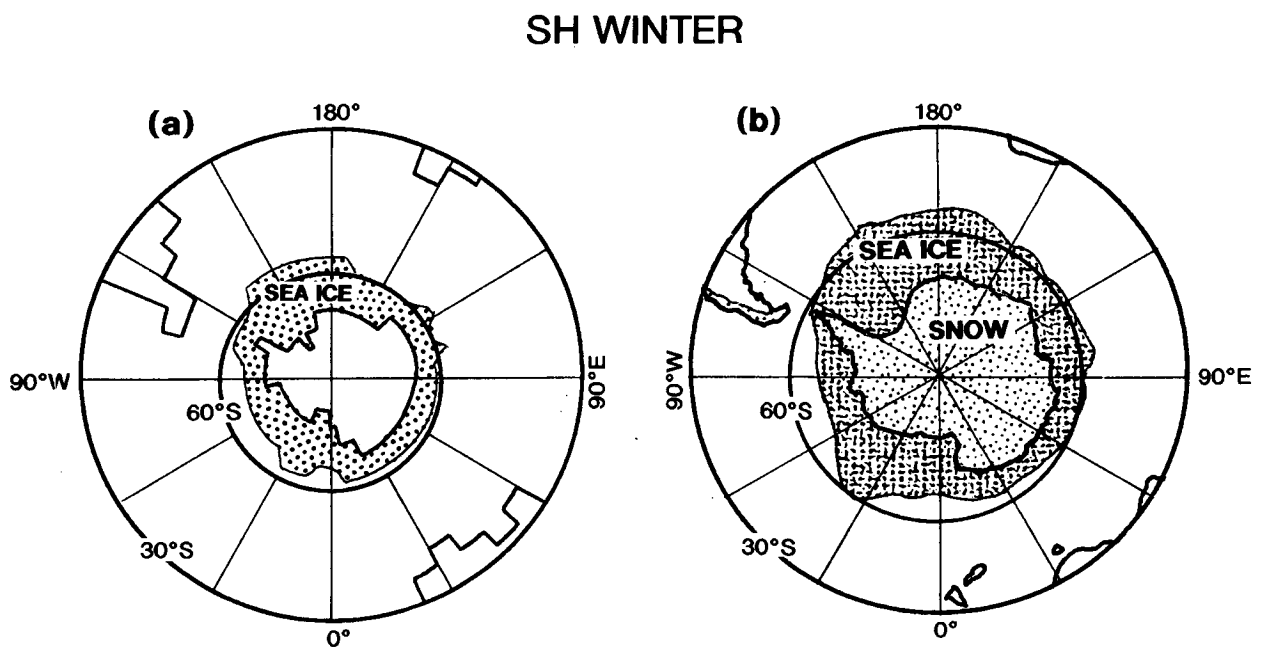

FIG. 3. As in Fig. 2 except for the Southern Hemisphere winter.

The overall performance of this model in simulating the present climate is not perfect but reasonable. It is noted that observations too are subject to uncertainties. Owing primarily to keeping cloud amounts and heights the same as in MB, and with LWP and r_e the same for each cloud height globally, biases in the "control" simulation are unavoidable. Because cloud amount, height, and properties are held fixed, there is no cloud-induced feedbacks in the experiments discussed below.

c. *Formulation of the experiments*

The perturbation experiments designed to address the issues posed in the introduction are summarized in Table 1 and described below:

(i) a globally uniform 37% increase in low-cloud LWP (experiment GLI)
(ii) a globally uniform 25% decrease in low-cloud LWP (experiment GLD)
(iii) a globally uniform 23% decrease in low-cloud r_e (experiment GRD),
(iv) a globally uniform 17% increase in low-cloud LWP (experiment GLI/2)
(v) a doubling of CO_2 from 300 to 600 ppmv (experiment $2\times CO_2$).

The changes in LWP or r_e above were derived by employing a one-dimensional radiative–convective model, with atmospheric profiles corresponding to the GCM's global annual-mean "control" climate, and by requiring the microphysical changes to yield a global annual-mean surface temperature change that is a specified multiple of that for $2 \times CO_2$. The appropriate tropopause forcing for $2 \times CO_2$ is listed in Table 1. Note that the global annual-mean forcing computed using a one-dimensional model with appropriate global annual-mean profiles is very similar to one from a latitudinally dependent evaluation (Ramaswamy and Chen 1993, hereafter RC).

Experiment GLI yields the same global-mean radiative forcing as a doubling of CO_2 but with the opposite sign. GLD yields the same sign and magnitude of forcing as a doubling of CO_2, that is, opposite to GLI. Experiments GLI and GLD thus are designed to investigate the invariance of the magnitude of the model response with respect to the sign of the radiative forcing. Experiments GLI and GLI/2 are designed to investigate the linearity of the response with respect to the strength of the forcing. GRD yields the same sign and magnitude of the global-mean forcing as GLI except as produced by a change in r_e rather than LWP. The range in LWP and r_e values owing to the considered perturbations is reasonable, being within present-day observational bounds (Greenwald et al. 1993; Han et al. 1994).

In each experiment, a substantial period of integration (~25 years) was required to establish a new equilibrium climate. Each simulation was then continued for an additional 10 years to provide an adequate sample for the analyses. The averages of the last 10 years in each experiment are taken to be the equilibrium responses. The sensitivity to albedo and CO_2 changes is investigated by comparing the response in each perturbation experiment with the "control" simulation.

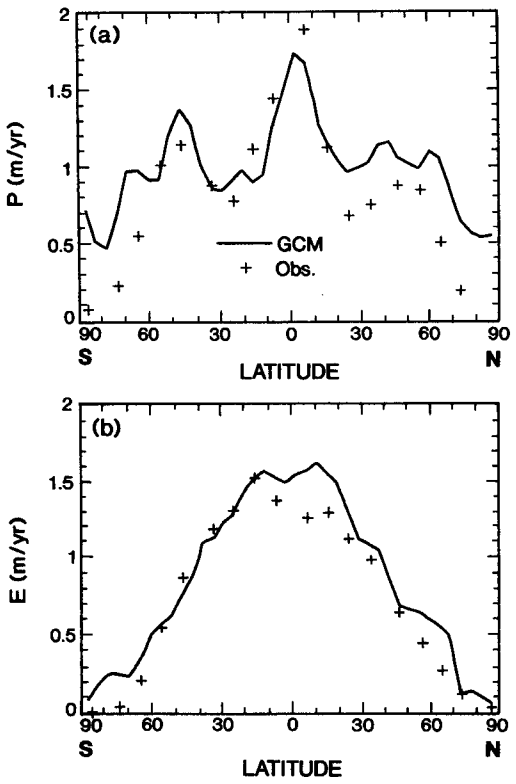

FIG. 4. Zonal annual-mean distribution of (a) precipitation and (b) evaporation rates.

d. *Zonal-mean radiative forcing*

Figure 5 shows the GCM's instantaneous "normalized" radiative forcing (zonal mean divided by the global mean listed in Table 1) for each experiment. Figure 5 highlights the relative strength in the latitudinal distribution of each forcing. The spatial patterns are similar for all the cloud perturbation experiments. The forcing is relatively greater in the tropical regions and in areas with large cloud amounts (RC). Near 60°S, the large cloud amount makes the forcing almost twice as large as the global annual mean. Though the globally averaged magnitude of the forcing in the cloud perturbation experiments (except GLI/2) is virtually the same as that due to doubling CO_2, the latitudinal dependence of these forcings, as pointed out by RC, is different. Also, the effect of a perturbation in cloud properties is "felt" mostly at the surface, but for 2 $\times$ CO_2 it is partitioned between the surface and troposphere.

3. Model results

a. *Thermal response*

The latitude–height distribution of the difference in the zonal-mean temperature between GLI and the "control" simulation is shown in Fig. 6a. The increase of LWP in this experiment causes less energy to become available in the global surface–troposphere system, resulting in a cooling. The cooling is particularly pronounced in the lowest layers in high latitudes (60°–90°) and is relatively smaller in the Tropics, despite the forcing being actually greater at the lower latitudes (Fig. 5). This results in a general increase of the meridional temperature gradient in the lower model tro-

TABLE 1. GCM experiments for studying the sensitivity of the model climate to globally uniform changes in low-cloud microphysical properties and to CO_2. The nominal values for low-cloud liquid water path (LWP) and effective radius are 80 g m^{-2} and 10 μm and are globally uniform.

Experiment	Perturbation in low cloud	Perturbation domain	Global annual-mean radiative forcing (W m^{-2})[a]
GLI	37% increase in LWP	global	−3.6
GLD	25% decrease in LWP	global	3.6
GRD	23% decrease in effective radius	global	−3.7
GLI/2	17% increase in LWP	global	−1.9
2×CO_2	—	global	3.7

[a] For the cloud microphysics experiments, the forcing is evaluated at the top of the atmosphere and is very nearly similar to that at the tropopause. For 2 $\times$ CO_2, the global annual-mean tropopause forcing is calculated using a one-dimensional radiative–convective model, with globally and annually averaged atmospheric profiles taken from the GCM's "control" climate.

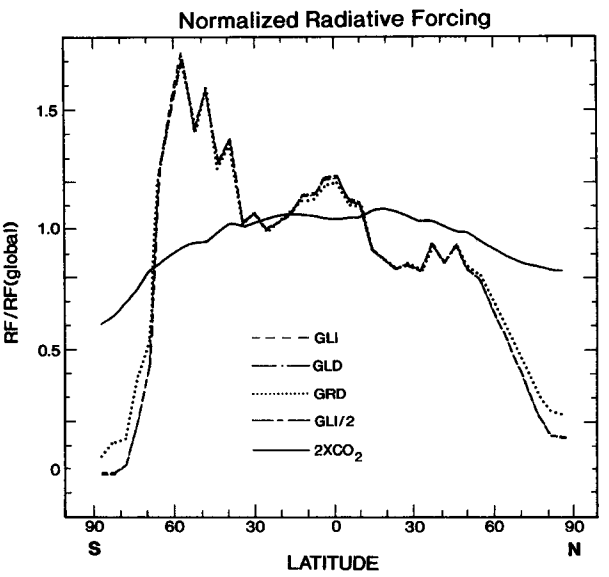

FIG. 5. Zonal annual-mean distribution of the normalized [zonal-mean, RF, divided by global-mean, RF (global)] radiative forcing in the GLI, GLD, GRD, GLI/2, and 2×CO_2 experiments.

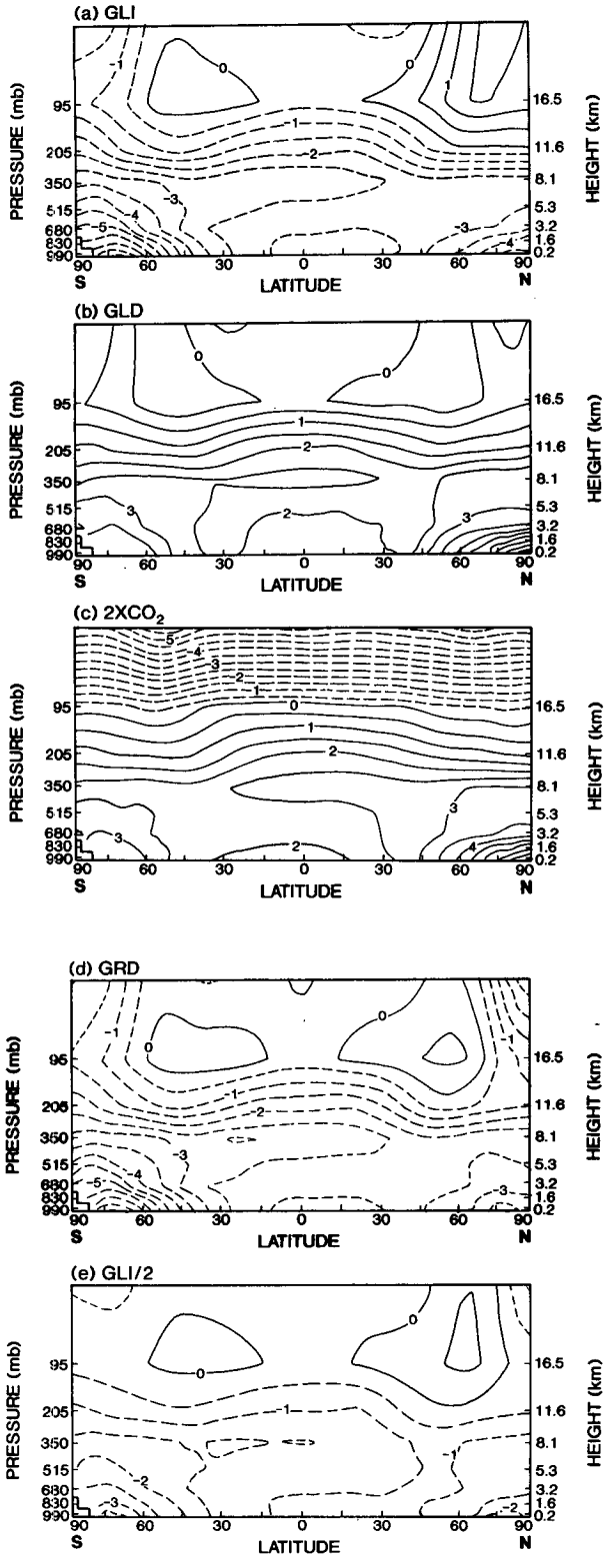

FIG. 6. Latitude–height distribution of the zonal annual-mean temperature changes in the (a) GLI, (b) GLD, (c) 2 × CO_2, (d) GRD, and (e) GLI/2 experiments.

posphere. There is an equatorward advance of the highly reflective snow surface and sea ice extent (Fig. 7). This, together with the large lower-tropospheric stability in the high latitudes, leads to a polar amplification of the temperature response in the lower troposphere (MS; Hansen et al. 1984). At low latitudes, there is a greater temperature decrease in the upper troposphere, despite the initial forcing being mostly felt at the surface. The upper-tropospheric maximum in the cooling reflects the following fact: if we start with two air parcels near the surface, one cooler and therefore likely to contain less water vapor, the difference in their temperature is amplified as the parcels travel upward, since less latent heat is released in the cooler parcel (MS; Hansen et al. 1984; Held 1993). It may be noted that the quantitative amplification of this warming with height in low latitudes is sensitive to the parameterization of convection and differs from model to model (Mitchell et al. 1987). In contrast to the general cooling of the troposphere, there is a small warming of the stratosphere in the Northern Hemisphere high latitudes and the Southern Hemisphere midlatitudes.

The global and hemispheric mean temperature responses in GLI are listed in Table 2. There is an interhemispheric asymmetry in the temperature response in GLI. This may be expected since the imposed forcing is larger in the Southern Hemisphere (Fig. 5), but this is not the entire explanation, as explained below.

Figure 6b shows the latitude–height distribution of the zonal-mean atmospheric temperature change in the GLD experiment. In this case, the decrease of LWP results in a global warming. The largest temperature changes occur at a similar location as in GLI except for a change in the sign. At both northern and southern high latitudes, different magnitudes of change occur in the GLD and GLI experiments. GLD shows a relatively larger surface temperature response in the northern polar region compared to that in the southern polar region. Note that the Southern Hemispheric mean forcing in GLD is actually larger than the Northern Hemispheric value (Table 2) due to greater cloud amounts (see RC). This is why, in the discussion of the GLI experiment, we argue that forcing is only part of the reason for the interhemispheric asymmetry found in the temperature response for that case.

The reason for an asymmetric response between the two polar regions is mainly attributable to the simulated sea ice thickness and extent in the model. The albedo of sea ice in the model changes only when its thickness varies between 0 and 1 meter. In the northern polar region, the sea ice thickness in the "control" is gradually reduced from more than 1 m at the pole to less than 20 cm at 60° ~ 70°. The seasonal variation of the sea ice thickness in the control run is shown in Fig. 8a. Note that only very limited sea ice forms along the Antarctic coast during summertime.

Figures 8b and 8c show the change in surface albedo accompanying the changes in sea ice for GLI and GLD,

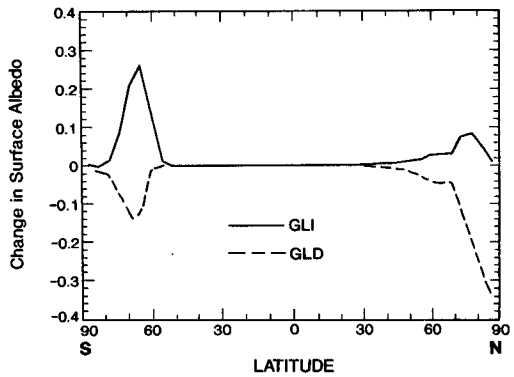

FIG. 7. Zonal annual-mean distribution of the surface albedo changes in the GLI and GLD experiments.

respectively. In GLD, the surface albedo of the northern polar region is reduced throughout the year, accompanying the changes in sea ice (Figs. 7 and 8c). Especially large decreases (more than −0.2) are found from June to February (Fig. 8c; large areas with sea ice thicknesses more than 1 m in the control become less than 1 m for GLD) and thus lead to a large zonal-mean albedo reduction (Fig. 7). The surface albedo change for a warmer climate near the Antarctic occurs mainly in the wintertime when the solar insolation is small. Because there is already less sea ice in the "control" during summer (Fig. 8a), a warming does not result in the melting of much sea ice nor change in albedo.

In contrast to GLD, a larger surface temperature response is found near the Antarctic than in the Arctic in GLI (Fig. 6a). When the surface temperature cools, the Antarctic sea ice advances equatorward from near the edge of the continent to approximately 60°S and induces a large increase in surface albedo there (Fig. 7); this occurs throughout the year, more so during the Southern Hemisphere summer (Dec, Jan, and Feb) and fall (Mar, Apr, and May) seasons (Fig. 8b). The sea ice in the northern polar region also grows in the GLI experiment. However, because these are areas with sea ice thicknesses more than 1 m and thus have reached a saturation of their surface albedo value, they are not affected greatly.

The hemispheric-mean temperature responses in GLD do not differ as much in the two hemispheres as they do in GLI (Table 2). Both the strength of the forcing and sea ice effects contribute to the respective hemispheric temperature responses. The more significant sea ice effect in the Northern Hemisphere (relative to the Southern) in GLD acts to compensate for the lesser initial radiative forcing in that hemisphere. This reduces the interhemispheric asymmetry, as gauged by the hemispheric-mean surface temperature response. Thus, the degree of interhemispheric asymmetry in each experiment and the opposite nature of this asymmetry in GLI and GLD are not only due to the magnitude of the hemispheric forcings but also depend on the changes in the sea ice extent with respect to that in the control climate. The importance of the control sea ice for climate sensitivity has been noted in earlier studies (Spelman and Manabe 1984; Hansen et al. 1984; Mitchell et al. 1987).

Figure 6c shows the latitude–height cross section of the temperature response in the $2\times CO_2$ experiment. Compared to GLD (Fig. 6b), the major difference is the well-known CO_2-induced stratospheric cooling (Manabe and Wetherald 1967). With a similar radiative forcing at the tropopause, the pattern of the temperature response in the troposphere is similar to that in GLD. Both show the largest surface warming in polar latitudes. The reason for the asymmetry in the interhemispheric surface temperature response at the high latitudes for $2\times CO_2$ is the same as discussed for GLD. The CO_2 experiment also shows an upper-tropospheric maximum in the warming over the tropical regions, similar to GLD. However, GLD shows a slightly greater increase in the Southern Hemisphere tropospheric temperatures. This is related to the larger Southern Hemisphere radiative forcing in GLD (Table 2; Northern Hemisphere: 3.1 W m^{-2}, Southern Hemisphere: 4.1 W m^{-2}). In the $2\times CO_2$ experiment, the radiative forcing at the tropopause is more uniform in the two hemispheres (~3.9 and ~3.8 W m^{-2} in the Northern and Southern Hemispheres, respectively;

TABLE 2. Changes in the annually averaged global (G), Northern Hemispheric (N), and Southern Hemispheric (S) mean surface-air temperature (T_S) and precipitation (P) for the GLI and GLD experiments. The values of T_S and P in the "control" run and that of the radiative forcing (ΔQ) in the two experiments are also listed.

	ΔT_S (K)			ΔP (cm yr^{-1})			ΔQ (W m^{-2})		
	G	N	S	G	N	S	G	N	S
GLI	−2.8	−2.2	−3.4	−8.1	−5.7	−10.6	−3.6	−3.1	−4.1
GLD	2.5	2.5	2.5	7.7	7.0	8.5	3.6	3.1	4.1
	T_S (K)			P (cm yr^{-1})					
Control	288.5	289.2	287.7	109.1	114.8	103.5			

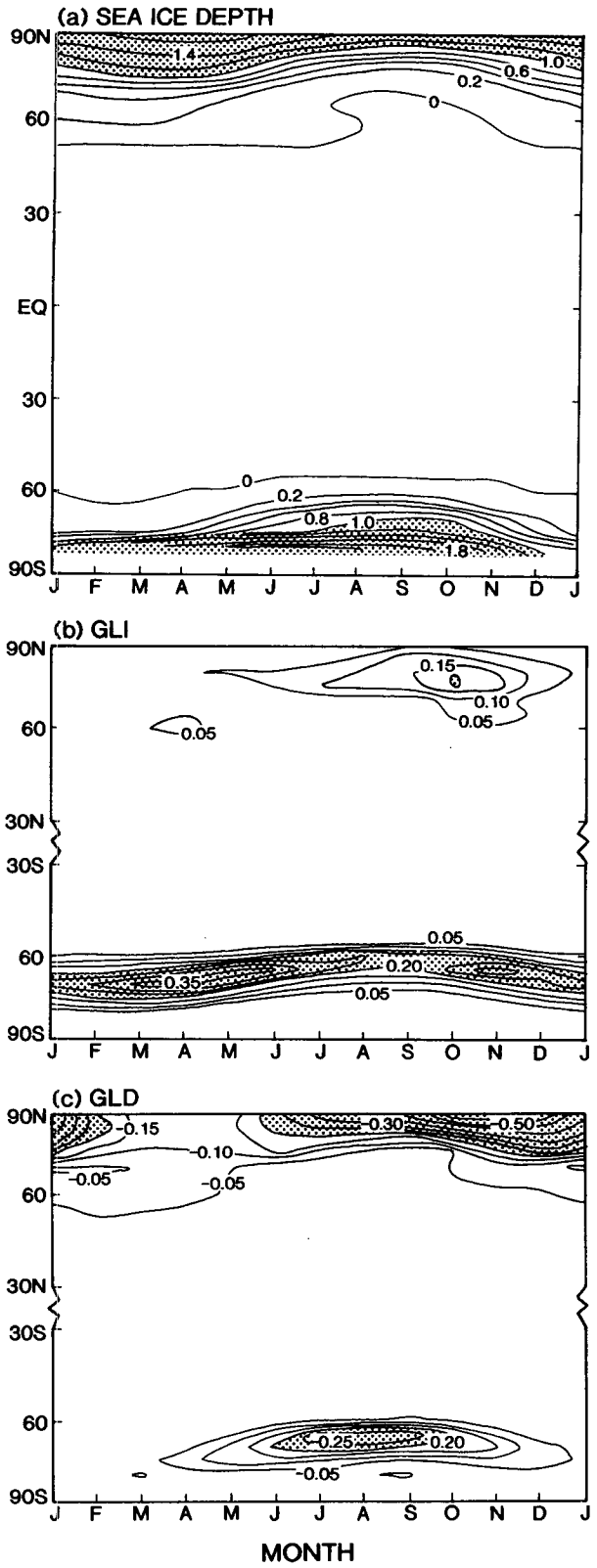

FIG. 8. Latitude–month distribution of (a) sea ice thickness (m) in the "control" simulation and the change in surface albedo in the (b) GLI and (c) GLD experiments.

these are obtained by adjusting the instantaneous forcings in the GCM with an additional flux change derived from a hemispheric radiative–convective model run that accounts for the new radiative equilibrium state of the stratosphere).

The temperature response in the GRD experiment is almost identical to that in GLI (Fig. 6d). Recall that the radiative forcing is very similar (<2%) in the two experiments (Table 1). However, the variations in r_e do not have the same impact on both cloud reflectivity and absorptivity as do the variations in LWP. That is, although we select the percentage changes in r_e and LWP in the two experiments, respectively, to yield similar changes in albedo and forcing, the changes in cloud and hence atmospheric absorption are not similar. In fact, this difference in cloud absorption leads to a 20% difference in the surface solar radiative flux. However, the model temperature responses do not reveal any significant differences. This indicates that, for the climate system as a whole, it does not matter much whether the globally uniform perturbation is caused by a change in LWP or r_e; what matters is the total surface–atmosphere forcing. A separation into a surface and troposphere forcing also does not seem necessary in the present context. Experiment GLI/2 resembles GLI in its zonal temperature response (Fig. 6e) except that the magnitude is reduced by about one-half. This suggests that the model's temperature response scales almost linearly with the forcing, at least if the sign of the forcing is the same.

As a means to evaluate the relative latitudinal pattern of the response, we introduce the normalized surface air temperature response. This is the zonal-mean temperature change divided by the global-mean value. In Fig. 9, we plot the normalized surface air temperature responses for all five GCM experiments. Note that the ratio yields a positive value and highlights the spatial distribution instead of the absolute value for each ex-

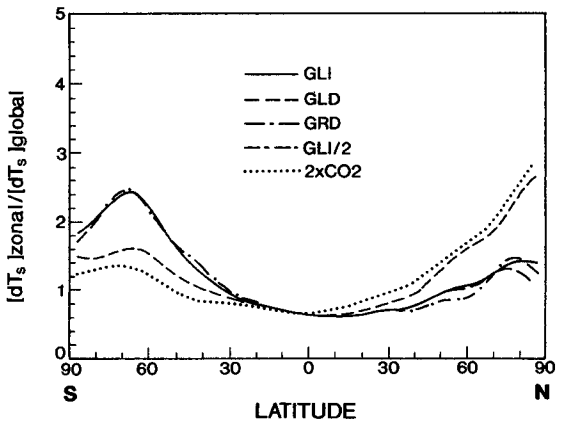

FIG. 9. Zonal annual-mean changes in the surface-air temperature divided by the global-mean change for the GLI, GLD, GRD, GLI/2, and $2\times CO_2$ experiments.

periment. The curves in the plot can be categorized into two distinct groups: (i) global uniform perturbation with negative forcing (GLI, GRD, and GLI/2) and (ii) global uniform perturbation with positive forcing (GLD and $2\times CO_2$). Several points may be summarized from Fig. 9.

- The normalized surface air temperature response near the equator is approximately similar for the various globally uniform perturbation experiments despite differences in the sign and magnitude of the forcings.
- There is an interhemispheric asymmetry in the normalized response at the high latitudes, with the two polar regions experiencing different magnitudes of change in each perturbation experiment. Furthermore, the normalized temperature in each polar region responds differently to forcings with the same magnitude but having opposite sign. As pointed out, the factors governing these features are the hemispheric magnitudes of the forcings and the changes in the sea ice extent and thickness in each hemisphere.
- The difference in the hemispheric forcings between GLD and $2\times CO_2$ leads to a slightly larger normalized response for GLD in the Southern Hemisphere and a slightly smaller value in the Northern Hemisphere.

b. Hydrologic response

We discuss the hydrologic response by focusing first on the results from the GLI experiment. There is a decrease in the global water-vapor mixing ratio consistent with the negative forcing and the global cooling (Fig. 10). The precipitation (P) and evaporation (E) rates in GLI are reduced over nearly all latitudes (Fig. 11a), with the global-mean changes (Table 2) in P indicating an ~7% decrease in the overall intensity of the hydrological cycle. The changes in P at the high latitudes are generally larger than those in low latitudes owing to the change in the meridional temperature gradient. This reduces the poleward moisture transport (Manabe and Wetherald 1975), thereby causing a marked reduction in the precipitation in the high latitudes. The latitudinal distribution of the decrease in E in GLI is quite different from that for P (Fig. 11b). The change in E decreases with increasing latitude and is relatively small at the high latitudes. Thus, the latitudinal distribution of the water balance at the earth's surface is significantly altered from the control run. This is made more

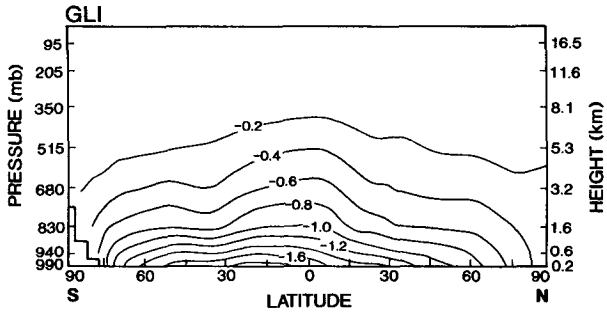

FIG. 10. Latitude–height distribution of the changes in the zonal annual-mean water vapor mixing ratio in the GLI experiment.

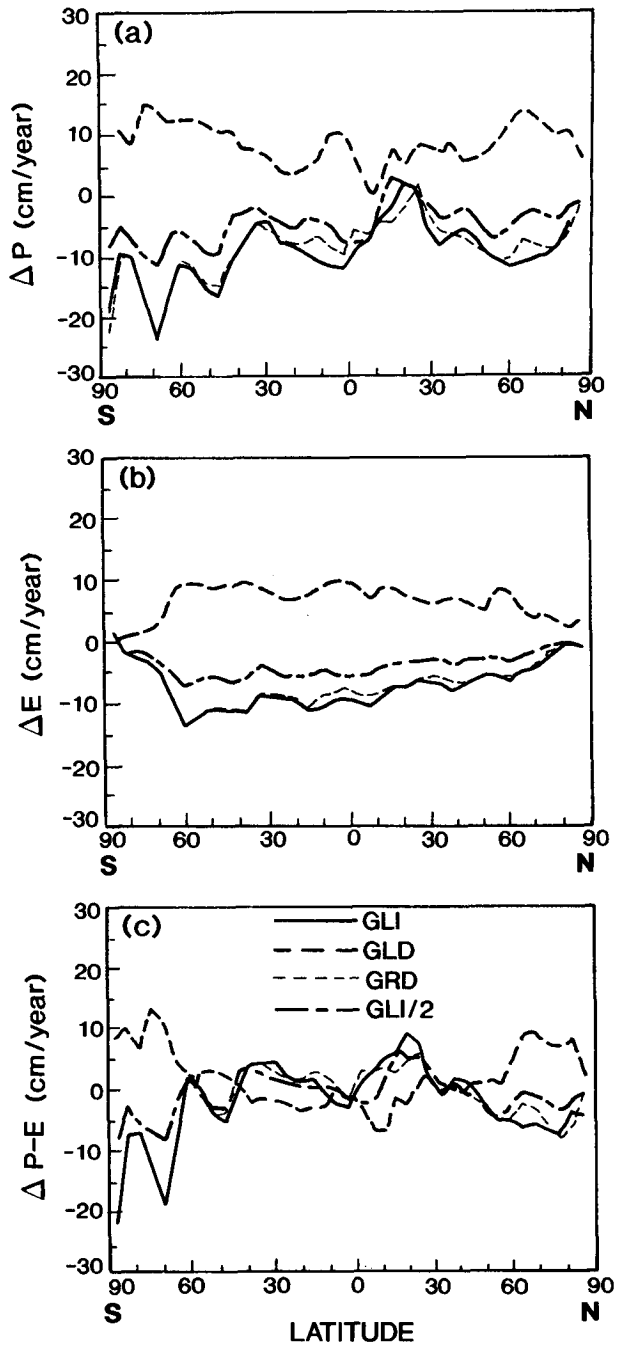

FIG. 11. Zonal annual-mean distribution of changes in the (a) precipitation rate, (b) evaporation rate, and (c) $P - E$ in the GLI, GLD, GRD, and GLI/2 experiments.

evident in Fig. 11c, which illustrates that the zonal-mean change in $P - E$, that is, the net water gain by the earth's surface, decreases at the high latitudes and increases at some of the lower latitudes.

Comparing the changes in P, E, and $P - E$ for the GLD, GRD, and GLI/2 experiments relative to GLI (Fig. 11), there is a consistency with respect to the sign and magnitude of the forcing. Relative to GLI, the changes in GRD are similar, while those in GLD have an opposite sign (see Table 2) and those in GLI/2 are reduced.

We next compare GLD with the $2\times CO_2$ experiment (Fig. 12). In the $2\times CO_2$ experiment, the increase in evaporation varies little with latitude, whereas the main increase in precipitation occurs in middle to high latitudes, in accordance with the Manabe and Wetherald (1975) study. Considering the global-mean P and E, the increase in the $2\times CO_2$ experiment is only 4.5%, while in the case of GLD (Table 2), the increase is about 7% (the global-mean surface temperature response is nearly same in both cases, ~2.5 K). Most of the differences in P and E between the two experiments come from the low and middle latitudes of the Southern Hemisphere (Fig. 12). The systematic differences in E can be explained from surface energy budget considerations (discussed in the next section). In contrast to the $2\times CO_2$ case, the change in the solar flux for cloud perturbations is "felt" mostly at the surface. Also, the change in the radiative flux at the surface for the $2\times CO_2$ experiment is smaller. The increase in latent heat flux loss (evaporation) required for the surface energy balance is hence smaller in the $2\times CO_2$ experiment. Considering the $P - E$ pattern, some of the individual differences in P and E become compensatory (Fig. 11c). The $P - E$ pattern also suggests that the poleward transport of moisture increases markedly in both experiments (cf. MS).

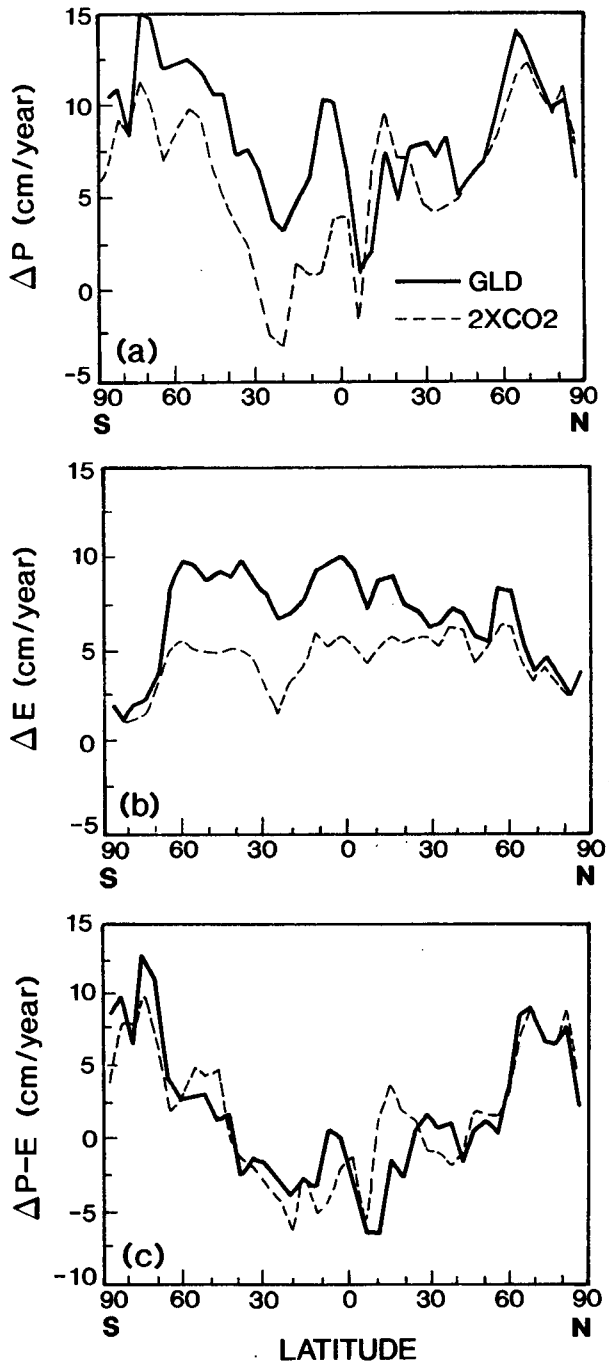

FIG. 12. Zonal annual-mean distribution of the change in the (a) precipitation rate, (b) evaporation rate, and (c) $P-E$ for the $2\times CO_2$ and GLD experiments.

c. *Maintenance of the surface energy budget*

We analyze next the terms contributing to the surface energy budget and the redistribution of these terms in the different perturbation experiments. The annual-mean surface energy budget equation in the model's basic state is given by

$$S + F + \mathrm{LE} + H \approx 0, \qquad (1)$$

where S is the net solar, F the net infrared, and LE the latent and H the sensible heat fluxes at the surface. The signs of the terms are positive if they warm the surface. The energy released by the melting and freezing of sea ice is much smaller than the other terms and is neglected. Oceanic heat transport is also not considered here.

Equation (1) can be written, using the terminology in Boer (1993), as

$$(S_0 - \sigma T_{\mathrm{sfc}}^4) + (G_{\mathrm{clr}} + W_{\mathrm{clr}}) + C_{\mathrm{LW}} + C_{\mathrm{SW}} + A_{\mathrm{sfc}} + \mathrm{LE} + H \approx 0, \qquad (2)$$

where S_0 is the global annual-mean solar radiation at the top, $\sigma T_{\mathrm{sfc}}^4$ is the blackbody surface emission, G_{clr} is the downward emission by the cloud-free atmosphere, and W_{clr} represents the solar absorption and scattering by gas molecules; C_{LW} and C_{SW} represent the longwave

and the shortwave cloud forcing at the surface, and A_{sfc} is the radiative effect due to surface albedo. The global-mean values of the terms in the model's control climate (Table 3) are within range of, or are approximately similar to, the observational estimates reported in Boer (1993).

The incident solar flux at the surface, S, can be decomposed into different components as shown in (2) and listed in Table 3. The absorption and scattering by gas molecules in the atmosphere (W_{clr}) is the most dominant term in reducing S_0 before sunlight can reach the ground, followed by the effect of clouds (C_{SW}), which contributes about 40% to the total sky shortwave effect. Most of the downward longwave flux is due to the downward emission by the cloud-free atmosphere (G_{clr}, mainly by CO_2 and H_2O) with the longwave cloud effect (C_{LW}) being small. This is because the cloud-free atmosphere is close to being opaque in the infrared due to the CO_2 and H_2O absorption lines and the H_2O continuum; the addition of a blackbody in the form of clouds does not contribute much more. This is in contrast to the dominant effect of clouds on the net radiative flux at the top of the atmosphere.

The perturbed surface energy budget at the new equilibrium can be written as

$$\delta S + \delta F + L\delta E + \delta H = 0. \quad (3)$$

The corresponding difference equation for (2) can be written as

$$-4\sigma T_{sfc}^3 \delta T_{sfc} + \delta G_{clr} + \delta W_{clr} + \delta C_{LW} + \delta C_{SW} + \delta A_{sfc} + L\delta E + \delta H = 0 \quad (4)$$

with

$$\delta F = \delta G_{clr} + \delta C_{LW} - 4\sigma T_{sfc}^3 \delta T_{sfc}, \quad (5)$$

$$\delta S = \delta W_{clr} + \delta C_{SW} + \delta A_{sfc}. \quad (6)$$

The globally annually averaged values of the difference terms for all the perturbation experiments are also listed in Table 3. Positive values imply a change acting to warm (increased input or decreased output) the surface, while negative values imply a change acting to cool the surface (decreased input or increased output).

In GLI, δS, δF, and δH all act to cool the surface; they are balanced by $L\delta E$, which acts to lessen the surface cooling. This new balance is obtained in association with cooler temperatures (Fig. 6a) and a less moist atmosphere (Fig. 10). The positive δW_{clr} is attributable to the drier atmosphere and lesser solar absorption by water vapor. The increase of cloud reflectivity in GLI (imposed forcing) is responsible for the large negative value of the change in the solar cloud effect δC_{SW}, while the surface albedo increase (Fig. 7) yields a negative δA_{sfc}. Here δF is negative just like δS but is slightly smaller in magnitude, and δG_{clr} is negative and greater in magnitude than $\delta(\sigma T_{sfc}^4)$. This is due to the decrease in the atmospheric temperature and effective emissivity as a result of the drier atmosphere. The decrease in the surface temperature causes a positive $\delta(\sigma T_{sfc}^4)$, that is, a decrease in surface emission. A decrease in the clear-sky emissivity tends to increase slightly the longwave surface cloud forcing (δC_{LW}).

Comparing GLD with GLI, the magnitude of the changes in each term is similar to that in GLI but with an opposite sign. The changes in the various energy terms in the GRD experiment are essentially similar to those in the GLI experiment except for δC_{SW}. This is mainly due to the differences in the cloud absorption between the two experiments, which leads to approximately 20% less change in the solar radiative flux at the surface for the GRD experiment. Comparing GLI/2 with GLI, the magnitude of the changes in each of the energy terms in GLI/2 is very close to one-half of that in GLI. Thus, the global annual-mean changes in the surface energy budget terms for these two cases exhibit a linear scaling with respect to the forcing.

In the $2 \times CO_2$ case, the new balance in the global-mean surface energy budget comes about through the

TABLE 3. Terms (see § 3d) making up the global and annual average surface energy budget (W m^{-2}) in the "control" run and the changes in the different perturbation experiments. The observational estimates "NAS" (Natl. Acad. Sci.) and "Budyko" are taken from Boer (1993).

		δX in the experiments						
X	Control	GLI	GLD	GRD	GLI/2	2×CO$_2$	NAS	Budyko
S	168.9	−3.6	3.2	−2.8	−1.8	−1.0	176	144
F	−62.8	−2.2	2.6	−2.4	−1.2	3.5	−73	−48
LE	−86.5	6.4	−6.1	6.0	3.2	−3.8	−79	−80
H	−15.0	−0.4	0.4	−0.7	−0.2	1.3	−24	−16
S_o	343.9	—	—	—	—	—		
W_{clr}	−86.1	2.5	−2.2	2.5	1.2	−2.7		
C_{SW}	−63.1	−4.4	4.3	−3.4	−2.3	−0.0		
A_{sfc}	−25.9	−1.7	1.2	−2.0	−0.7	1.7		
G_{clr}	320.4	−18.3	17.6	−18.7	−9.2	17.9		
C_{LW}	28.4	1.7	−1.7	1.7	0.8	−1.8		
σT_{sfc}^4	−411.6	14.5	−13.3	14.6	7.2	−12.7		

increase and decrease, respectively, of latent heat and longwave flux losses. Lesser but nonnegligible changes occur in the solar and the sensible heat fluxes. The changes in the terms are quite different from those in the GLD experiment, which has the same global-mean forcing. A substantial difference is seen in the net surface radiative flux change (2.5 vs 5.8 W m^{-2}) in the two experiments. This may be explained as follows: the instantaneous doubling of CO_2 increases the net surface radiative flux (global mean ~0.6 W m^{-2}, from off-line radiative transfer calculations). In contrast, the reduction of the cloud LWP in the GLD experiment, an effect which is felt mostly at the surface, increases the surface radiative flux by 3.8 W m^{-2}. This initial difference is the main reason for the differences in the net surface radiative flux at the new equilibria in the two experiments. It is a manifestation of the fact that the forcing in GLD is felt almost exclusively at the surface. That the partitioning of the forcing between surface and troposphere plays a key role in the surface energy budget is supported by the results for GLD and GLI, which have forcings of opposite signs but are "felt" directly at the surface, and experience changes in the terms (Table 3) that are of approximately similar magnitude.

In contrast to the changes in the surface energy budget, the influence of the atmosphere is quite similar in both the GLD and $2\times CO_2$ experiments (W_{clr}, G_{clr}, C_{LW}). This is because the temperature and moisture responses in the two experiments are quite similar, namely, a warmer and more moist atmosphere. Relative to GLD, the smaller increase in surface radiative flux input in the $2\times CO_2$ experiment is accompanied by a larger reduction in sensible heat output and a smaller increase in latent heat flux output. The overall vigor of the hydrologic cycle (P and E) in the $2\times CO_2$ experiment is, therefore, weaker than that in GLD (section 3b).

Thus, even though the surface temperature responses in the $2\times CO_2$ and GLD experiments are very similar, the similarity of the new thermal equilibrium state is reached through different changes in the terms contributing to the surface energy budget. The changes in the zonal-mean and global-mean precipitation rates are linked to the differences in the surface energy components. This implies that the impact on hydrological processes may not be the same in the instance of trace gas increases versus changes in cloud radiative properties, despite a similarity in their respective global-mean surface temperature responses.

4. Feedback analyses

a. Method

Next, we analyze the role of the feedback processes in governing the changes to the climate system as a whole. For this purpose, we consider the TOA radiative balance. Since cloud distribution and properties are fixed in the perturbation experiments, there are no cloud-induced feedbacks and the analysis is concerned only with the noncloud feedback processes. The global annual-mean surface air temperature change (ΔT_s) can be written as (Schlesinger 1988, 1989)

$$\Delta T_S = \frac{G_0}{1 - \sum_j f_j} \cdot \Delta Q, \tag{7}$$

where ΔQ is the global annual-mean forcing and f_j denotes the jth feedback;

$$f_j = G_0 \cdot \frac{\partial N}{\partial I_j} \cdot \frac{dI_j}{dT_s} \tag{8}$$

with I_j representing the jth internal variable of the climate system and N the net (solar plus longwave) flux at the top of the atmosphere. From Eq. (8), the feedback due to a physical process j depends on (i) the sensitivity of the net flux N to the variable I_j as given by $\partial N/\partial I_j$, (ii) the sensitivity of the variable to the surface-air temperature as given by dI_j/dT_s, and (iii) the zero-feedback gain of the climate system G_0.

The planetary radiative energy budget can be written as

$$N = \frac{(1 - \alpha_p)}{4} S_0 - \varepsilon\sigma T_s^4, \tag{9}$$

where S_0 is the solar constant, α_p the planetary albedo, ε the effective emissivity of the earth–atmosphere system, and σ the Stefan–Boltzman constant. Then, the zero-feedback gain is given by (Schlesinger 1989) as

$$G_0 = -\left(\frac{\partial N}{\partial T_s}\right)^{-1} = \frac{1}{4\varepsilon\sigma T_s^3}. \tag{10}$$

Here G_0 is calculated as follows. In the "control" simulation, the global-mean surface air temperature, T_s = 288.5 K. From the equation for the longwave flux emission (viz. $\varepsilon\sigma T_s^4$), we obtain the effective planetary emissivity ε as 0.603. Equation (10) then gives a zero-feedback gain G_0 as 0.305 K W^{-1} m^{-2} (see also WM).

Following WM, we rewrite Eq. (8) as

$$f_j = G_0 \cdot \frac{\partial N}{\partial I_j} \cdot \frac{dI_j}{dT_s} = G_0 \cdot \frac{[\delta_j N]}{[\Delta T_s]}, \tag{11}$$

where $[\delta_j N]$ is the global-mean change in the net radiation at the top of the atmosphere due to feedback process j and $[\Delta T_s]$ is the change in the global-mean surface air temperature. The notation here is different from WM; their parameters λ_0 and λ_j are transformed to $1/G_0$ and $-f_j/G_0$, respectively (Schlesinger 1988).

The strategy employed is as follows: The radiative transfer algorithm in the GCM and the monthly mean quantities over the period of an annual cycle for both the "control" and the "perturbation" GCM simulations are considered. For each month, the monthly mean geographical distributions of the relevant climate

TABLE 4. $[\delta_j Y]$ (in W m^{-2}) and $[\Delta T_s]$ (in K) for the different experiments. SW: net downward solar flux, LW: upward longwave flux, N: net radiative flux at the top of the atmosphere, T: surface-air temperature change, r: water vapor, A: surface albedo. All quantities are global, annual means.

	j		
Y	T	r	A
	GLI ($[\Delta T_S]$ = −2.8 K)		
SW	−0.2	−0.6	−1.5
−LW	8.7	−2.0	—
N	8.5	−2.6	−1.5
	GLD ($[\Delta T_S]$ = 2.5 K)		
SW	0.4	0.6	1.7
−LW	−8.4	2.0	—
N	−8.0	2.6	1.7
	GRD ($[\Delta T_S]$ = −2.9 K)		
SW	−0.2	−0.6	−1.6
−LW	8.9	−2.1	—
N	8.7	−2.7	−1.6
	GLI/2 ($[\Delta T_S]$ = −1.4 K)		
SW	−0.1	−0.3	−0.8
−LW	4.4	−1.1	—
N	4.3	−1.4	−0.8
	2×CO$_2$ ($[\Delta T_S]$ = 2.5 K)		
SW	0.4	0.6	1.7
−LW	−7.4	2.0	—
N	−7.0	2.6	1.7

quantities for the control simulation are used in the radiation code, and the geographical distribution of N is calculated. The resulting 12 sets of values for N are then globally and annually averaged. Then, for any specific perturbation experiment, the above radiative computation and the averaging process are repeated, separately for each feedback process, by replacing the monthly mean quantity from the GCM control run with the corresponding quantity from the perturbation experiment. The difference between the two calculations yields $[\delta_j N]$ for the jth feedback process.

b. *Results*

1) CLOUD MICROPHYSICS EXPERIMENTS

The feedbacks in the perturbation experiments are due to changes in temperature, water vapor, and surface albedo. Table 4 lists the values of $[\delta_j N]$ and $[\Delta T_s]$ for the different experiments. The changes in the TOA net flux N are subdivided into the net downward solar (SW) and the net upward longwave (LW) components; $j = T$, r, and A identify, respectively, the changes in the TOA fluxes due to changes in temperature, water vapor, and surface albedo.

In general, the effect of changes in T in the warming (cooling) experiments leads to a global-mean decrease (increase) of the net radiative flux into the surface–atmosphere system. Changes in water vapor and albedo influence the TOA radiative fluxes in a sense opposite to that due to temperature changes. The longwave flux changes dominate the solar ones. The magnitude of the radiative flux changes in GLI and GLD due to temperature, water vapor, or surface albedo changes are all approximately similar, as are their global-mean forcings (Table 1) and surface temperature responses. GRD has similar flux changes as GLI, confirming the near independence of the global-mean response to a change in LWP or r_e. Flux changes in GLI/2 are about one-half of those in GLI, emphasizing a linear scaling of the global-mean results with respect to the imposed forcing.

The magnitude of the feedbacks due to water vapor and surface albedo are computed using Table 4 and Eq. (11) and are listed in Table 5. An implicit assumption in the feedback analyses is the linear additivity and independence of the mechanisms from each other. For each experiment, the total feedback $f(\Sigma f_j)$ is obtained using Eq. (7), with ΔQ (radiative forcing) from Table 1 and $[\Delta T_s]$ from Table 4. We then compute the residual between the total feedback and the sum of the water vapor and surface albedo feedbacks. Provided that the independence and additivity assumptions employed in the feedback analyses hold true, this residual can be identified as the temperature lapse rate feedback. Accordingly, we will term the residual the "lapse rate" feedback (Table 5), recognizing that a direct computation of this term (as in WM) could yield a different value.

The gain of the climate system with feedbacks, G_f, is given by

$$G_f = \frac{G_0}{1 - \sum_j f_j}. \tag{12}$$

Here G_f is also referred to as the global-mean climate sensitivity factor, leading to a simple relation between

TABLE 5. Feedback factor f and the gain of the climate system with feedbacks in the different GCM experiments.

Feedbacks	GLI	GLD	GRD	GLI/2	2×CO$_2$
Water vapor	0.28	0.31	0.28	0.32	0.32
Surface albedo	0.17	0.21	0.17	0.18	0.21
Lapse rate	0.15	0.04	0.15	0.09	0.02
Total	0.60	0.56	0.60	0.59	0.55
Gain of the climate system with feedbacks	0.76	0.69	0.76	0.74	0.68

the equilibrium global annual-mean change in surface temperature and the global annual-mean radiative forcing (i.e., $\Delta T_s = G_f \Delta Q$).

The climate sensitivity factor (Table 5) is seen to be similar for the different experiments (0.69–0.76 K W^{-1} m^{-2}). That is, the total feedback occurring in each experiment in response to the initial forcing is approximately the same in the global-mean context. The magnitude of the global annual-mean surface temperature response of the climate system is approximately independent of the sign and strength of the radiative forcing, at least as imposed in this study. In addition to the invariance property, the global-mean response scales almost linearly with the global-mean forcing. The uniformity of the global-mean surface temperature sensitivity in the various experiments exists in spite of the differences that can occur in the zonal response patterns (Fig. 9). Notwithstanding the above inference regarding the global climate sensitivity, the strengths of the individual feedback processes differ significantly between the various experiments. In all the experiments, the water vapor feedback is the strongest process (Table 5), consistent with Cess et al. (1990).

In GLI, the surface albedo and the lapse rate feedbacks yield similar contributions to the total feedback, while in GLD, the surface albedo feedback is larger. Compared to GLI, GLD has a small lapse rate but larger water vapor and surface albedo feedbacks. The lapse rate feedback in GLD includes the response of the stratosphere, which makes the total lapse rate feedback positive (WM), whereas, for the troposphere alone, it should be negative. This follows from the fact that the warming causes a reduction of the moist adiabatic lapse rate, making the upper layers of the troposphere warmer with respect to the increase in the zonal-mean surface temperature, especially in the Tropics (Fig. 6b, section 3b). This makes it possible for the system to restore equilibrium through a smaller change in surface temperature. Even though the differences in albedo feedback lead to interhemispheric asymmetries of an opposite nature in the high-latitude temperature responses of GLI and GLD, their normalized tropical troposphere temperature responses are similar (Fig. 9). The smaller magnitude of the global temperature response in GLD is likely due to the lapse rate effect since the other feedbacks are greater in this case (Table 5).

The larger surface albedo feedback in GLD relative to GLI is because the changes in GLD are greater in the Northern Hemisphere middle and high latitudes (Fig. 7, section 3b). Note that, in the Southern Hemisphere high latitudes, there is a larger change in the surface albedo for the GLI experiment. However, a factor that reduces the effect of the surface albedo feedback in GLI is the large low-cloud amount present in this area of surface albedo change (by contrast, in GLD a greater surface albedo change occurs in Northern Hemisphere high latitudes where the cloud amount is not as large). A larger cloud cover diminishes the effect of the surface albedo change on the net solar flux absorbed by the climate system (RC).

The changes in the water-vapor mixing ratio and global-mean surface temperature in GLD and GLI explain the different strengths of the water vapor feedbacks in these two experiments. Figure 13a shows the zonal-mean changes in the water vapor mixing ratio near the surface in these experiments. Although the magnitude of temperature change in GLD (ΔT_s = 2.5 K) is smaller than that in GLI (ΔT_s = −2.8 K), the amount of water vapor change in GLD can be expected to be greater at low latitudes on the basis of the Clausius–Clapeyron equation. However, the actual value of the water-vapor mixing ratio is also affected by the dynamical and hydrological processes in the model. In GLD, the magnitude of the change in low-level water-vapor mixing ratio is more than that in GLI in the Northern Hemisphere, but less in the Southern Hemisphere. Figure 13b shows the zonal-mean changes in the surface water-vapor mixing ratio divided by the

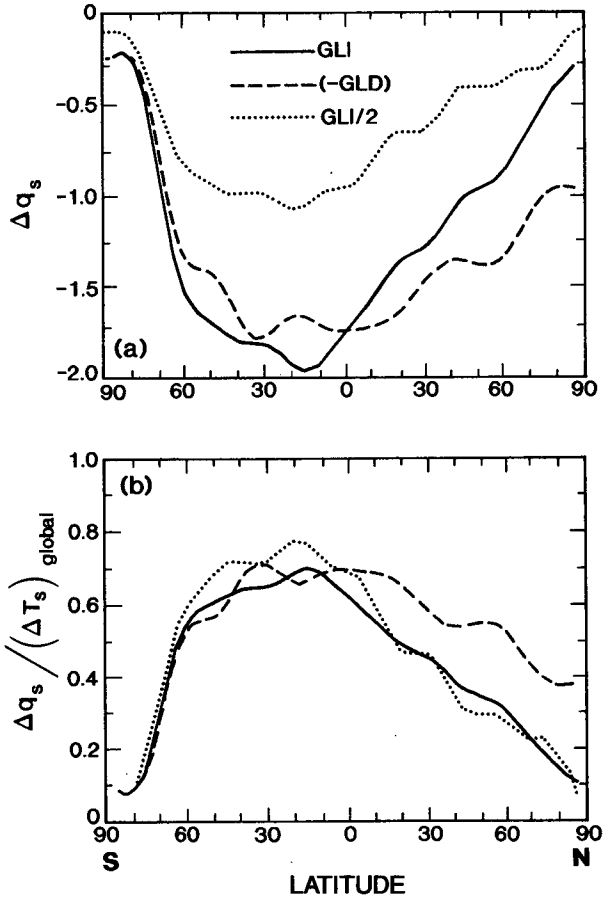

FIG. 13. Zonal annual-mean distribution of (a) changes in the water vapor mixing ratio near the surface (Δq_s) and (b) changes in the water vapor mixing ratio near the surface divided by the global-mean temperature response, $\Delta q_s/[\Delta T_s]_{global}$ in the GLI, GLD, and GLI/2 experiments.

global-mean surface temperature response for these experiments. This ratio illustrates that the greater water vapor feedback in GLD, in a qualitative sense, is mostly due to the larger change occurring in the Northern Hemisphere.

The similarity of the feedbacks in GLI and GRD is striking (Table 5), with the strength of each individual process being essentially identical. This reiterates strongly the close coupling between the surface and troposphere in the GCM and the indistinguishability of the responses due to changes in LWP or r_e. This comparison also emphasizes the fact that the forcing at the top of the atmosphere (or equivalently, in the present context, the tropopause) is appropriate for a comparative examination of GCM temperature responses, at least in the case of a globally uniform perturbation in the cloud microphysical properties.

Compared with GLI, GLI/2 has a slightly larger water vapor and surface albedo feedback, but the lapse rate feedback is smaller. The ratio shown in Fig. 13b indicates that the cause of the larger water vapor feedback in the GLI/2 experiment is mainly due to the larger ratio in the Southern Hemisphere low and middle latitudes. This is different from the cause of the larger water vapor feedback in the GLD experiment. The global-mean changes in the net radiative flux due to water vapor for the GLI/2 experiment are slightly greater than one-half of the GLI results (Table 4), consistent with the sense obtained from the Clausius–Clapeyron equation.

2) $2\times CO_2$ EXPERIMENT

We next perform a feedback analysis for the $2\times CO_2$ experiment. For a comparable analysis, we will now use the forcing at the tropopause, $[\Delta Q_{\text{TROP}}]$, instead of $[\Delta Q]$ at the top (cf. §4a). This is because (i) the sign of the CO_2-induced change in the stratosphere is opposite to that of the tropospheric and surface temperature changes and (ii) the changes in the stratospheric quantities (e.g., temperature) have a small effect on the tropospheric and surface temperatures (Schlesinger 1988). $[\Delta Q_{\text{TROP}}]$ is estimated using a radiative–convective model. For $2 \times CO_2$, the net flux change at the tropopause is 3.7 W m^2 (Table 1). Although this estimate is not strictly applicable in the context of a GCM, it is a more appropriate radiative forcing value than that computed at the top of the atmosphere.

Table 4 lists the value of $[\delta_j N]$ as computed for the $2\times CO_2$ GCM experiment. Now, $[\delta_j N]$ at the tropopause is estimated by assuming that $[\delta_j N_{\text{TROP}}] \approx [\delta_j N]$ at the top for the water vapor ($j = r$) and surface albedo ($j = A$) feedbacks. Since the effect of the surface albedo change on the solar flux at the tropopause is essentially the same as at the top of the atmosphere, we can readily estimate f_{albedo} by using $[\delta_A N]$ from Table 4. The change in the water-vapor mixing ratio is also mostly confined to the lower troposphere. Therefore, for the variation in the water-vapor mixing ratio, the net flux change at the tropopause is very similar to that at the top of the atmosphere; $f_{\text{water vapor}}$ is estimated using $[\delta_r N]$ from Table 4. The total feedback is calculated from Eq. (7) using the estimated $[\Delta Q_{\text{TROP}}]$ and the GCM-derived $[\Delta T_s]$. The residual (lapse rate feedback) is then obtained by substracting the sum of f_{albedo} and $f_{\text{water vapor}}$ from the total feedback f.

The gain of the climate system with feedbacks for $2 \times CO_2$ is quite similar to that for all the cloud experiments and is similar to that for GLD (Table 5). The quantitative aspects of the individual feedback processes in the $2\times CO_2$ experiment are also approximately the same as those in GLD. This suggests that the global-mean surface temperature response is the same if the global-mean forcings of these two types of perturbations are similar, no matter how different the spatial and temporal patterns of their forcings may be (Fig. 5). The response is similar whether the initial forcing is mainly at the surface (as for GLD) or distributed in both the atmosphere and surface (as for $2\times CO_2$). Thus, the partitioning of the forcing between the surface and troposphere is not particularly relevant for the global-mean response, at least in the framework of the GCM experiments performed in this study and from the TOA global annual-mean energy balance perspective. In contrast to the other experiments, the relatively small lapse rate feedback accounts for the slightly smaller sensitivity parameter in the case of both $2 \times CO_2$ and GLD.

5. Summary

The goal of this GCM (atmosphere coupled to a static mixed layer ocean) study has been to determine the sensitivity of the climate system to globally uniform perturbations in the microphysical properties (liquid water path or effective radius) of low clouds. This is tantamount to a study of planetary albedo perturbations. For comparison, a $2\times CO_2$ experiment is also performed, which is a greenhouse perturbation. Cloud properties are held fixed for all simulations so that there are no cloud feedbacks. The major inferences from the GCM experiments are as follows.

- The global-mean surface temperature response is determined, to a high degree of approximation, simply by the global-mean radiative forcing. The global climate sensitivity parameter (i.e., global-mean surface temperature divided by the global-mean radiative forcing) is almost independent of the sign, magnitude, and spatial distribution of forcing. Thus, within the context of the forcings studied, the model's global-mean response exhibits properties of invariance and linearity with respect to the radiative forcing.
- Although the total gain of the modeled climate system with *all* the feedbacks included is very similar in all the experiments, the magnitudes of the *individual*

feedback processes (e.g., water vapor, surface albedo) can be different, particularly between positive and negative radiative forcings.

- Changes in moisture, sea ice extent and thickness, and atmospheric static stability accompany the latitudinal and seasonal distribution of the surface temperature response. As a consequence, the equator-to-pole pattern of the response differs significantly from that of the imposed radiative forcing.

The global-mean and, to an approximate extent, even the pattern of the zonal-mean surface temperature responses for the $2\times CO_2$ and the cloud liquid water decrease (equivalent to an albedo decrease) experiments are similar despite there being a dissimilarity in the spatial distribution of their respective radiative forcings. This feature is reminiscent of earlier GCM studies that found the surface temperature responses to a 2% solar constant increase and carbon dioxide doubling to be similar (Wetherald and Manabe 1975; Hansen et al. 1984). The stratospheric response, however, is different in the two experiments since, unlike the $2 \times CO_2$ case, there is no stratospheric radiative forcing in the cloud albedo experiment.

The global climate sensitivity parameter for the various experiments has a range of only about 10% (0.68–0.76 K/W m^{-2}). It is slightly less in the perturbation experiments that lead to a warmer climate. In each experiment, there is an interhemispheric asymmetry in the magnitude of the high-latitude albedo feedback mechanism that is related to differences in the hemispheric forcing and, more significantly, to changes in sea ice thickness and extent in the two polar regions. The nature of this asymmetry is different for positive and negative forcings. The climate sensitivity parameter remains the same whether the perturbation is in cloud LWP or r_e (such that they yield the same change in the optical depth). When the globally uniform cloud microphysics-induced radiative forcing is reduced by one-half, the global temperature response also scales down by almost a factor of 2. Both the cloud microphysics and $2\times CO_2$ experiments emphasize that, as far as the global-mean surface temperature response is concerned, the global surface–troposphere forcing consideration is adequate, and it is not necessary to inquire into the details of the partitioning between the surface and the troposphere. As noted, the stratospheric temperature changes, however, are quite distinct for the $2\times CO_2$ experiment.

The latitudinal change in the model temperature response for all experiments is nonuniform. A crucial role is played by the feedback processes in determining the spatial distribution of the surface temperature response. The strengths of water vapor and surface albedo feedbacks for positive forcings exceed those for the negative ones. However, the residual between the total feedback and the sum of the water vapor and albedo feedbacks has a relatively smaller value for the positive forcings. The feedback processes make the horizontal and vertical response patterns different from those of the imposed radiative forcing. Thus, the present experiments suggest that the climate response to global-scale perturbations mask the spatial details of the forcing. In contrast to the climate sensitivity parameter that relates the global-mean surface temperature response and global-mean forcing, it does not seem meaningful to link the zonal-mean surface temperature changes with the zonal-mean forcing. However, a normalized zonal temperature response parameter (zonal-mean surface temperature change divided by the global-mean change) can be considered. In terms of this parameter, the spatial patterns from experiments with a perturbation that leads to a "colder" climate (negative forcing) are found to be nearly similar at all latitudes (Fig. 9). The same is true for the experiments with a global perturbation leading to a "warmer" climate (positive forcing), although the spatial patterns in this case differ from those for the negative forcing experiments.

The surface budget analyses show that the changes in the magnitudes of the terms making up the surface energy balance are different for the $2 \times CO_2$ and cloud LWP decrease experiments. Although both experiments have a similar temperature response, the partitioning of the radiative forcing between the troposphere and the surface is different. This results in different magnitudes of changes in the evaporation and precipitation rates, leading in turn to differences in the vigor of the hydrologic cycle between the two experiments. In general, the changes in the precipitation and evaporation rates for the different experiments are consistent with the sign and magnitude of the applied forcings.

The findings here strongly suggest that, if cloud feedbacks are absent or negligible, the global-mean surface temperature response due to globally uniform perturbations in cloud liquid water path or effective radius can be simply estimated by the global-mean radiative forcing. These values may be directly compared to those for increases in CO_2 and the other trace gases since, in both cases, the global-mean climate sensitivity factors are nearly similar. However, such a simple link of the response to the forcing does not extend, in general, to the zonal temperature response, hydrologic cycle response, or rearrangements in the surface energy balance. The above arguments can be extended to other types of global albedo forcings, for example, aerosol-induced albedo changes since, in these cases too just as for cloud microphysical changes, the forcings are felt mainly at the surface, and the spatial and temporal patterns of the forcing are governed by the solar insolation (RC).

The above inferences have to be considered in the framework of the present model and experiments. The deficiencies in the simulation of sea ice and the surface temperature at the high latitudes in the model's control climate could be affecting the response in the polar

regions. The conclusions here are limited to globally uniform fractional changes in cloud microphysics. Lines of future research instigated by this study include the following: Why, for different sign and strength of the forcings, the total feedback tends to be similar? To what extent do the seemingly invariant nature of the climate sensitivity parameter and the spatial pattern of the normalized zonal temperature responses depend on the model physics employed? How would consideration of cloud feedbacks affect the present conclusions? If, indeed, cloud feedbacks alter the characteristics of the responses shown here in a drastic manner, that would further heighten the role of clouds in governing climate processes. Likewise, the effects of other physical factors, such as oceanic heat transport and convection, also need to be examined. It would be interesting to test whether other models with different control climates, cloud amounts, and physical parameterizations lead to similar results. Further GCM studies ought to explore the answers to these questions, which would lead to a more thorough understanding of the climate effects due to albedo changes induced by changes in cloud microphysics.

Acknowledgments. We thank L. J. Donner, J. D. Mahlman, and S. Manabe for their invaluable suggestions; A. Broccoli and R. Wetherald for their assistance with the GCM; and C. Raphael and J. Varanyak for their help with the figures. We are also grateful to the anonymous reviewers for their helpful comments.

REFERENCES

Baumgartner, A., and E. Reichel, 1975: *The World Water Balance: Mean Annual Global Continental and Maritime Precipitation, Evaporation and Runoff.* Elsevier, 179 pp. + 31 pp. of maps.

Betts, A. K., and Harshvardhan, 1987: Thermodynamic constraint on the cloud liquid water feedback in climate models. *J. Geophys. Res.,* **92,** 8483–8485.

Boer, G. J., 1993: Climate change and the regulation of the surface moisture and energy budget. *Climate Dyn.,* **8,** 225–239.

Cess, R. D., G. L. Potter, J. P. Blanchet, G. J. Boer, A. D. Del Genio, M. Deque, V. Dymnikov, V. Galin, W. L. Gates, S. J. Ghan, J. T. Kiehl, A. A. Lacis, H. Le Treut, X.-Z. Liang, B. J. McAvaney, V. P. Meleshko, J. F. B. Mitchell, J.-J. Morcrette, D. A. Randall, L. Rikus, E. Roeckner, J. F. Royer, U. Schlese, D. A. Sheinin, A. Slingo, A. P. Sokolov, K. E. Taylor, W. M. Washington, R. T. Wetherald, I. Yagai, and M.-H. Zhang, 1990: Intercomparison and interpretation of climate feedback processes in 19 atmospheric general circulation models. *J. Geophys. Res.,* **95,** 16 601–16 615.

Charlson, R. J., J. E. Lovelock, M. O. Andreae, and S. G. Warren, 1987: Oceanic phytoplankton, atmospheric sulfur, cloud albedo and climate. *Nature,* **326,** 655–661.

——, S. E. Schwartz, J. M. Hale, R. D. Cess, J. A. Coakley Jr., J. E. Hansen, and D. J. Hofmann, 1992: Climate forcing by anthropogenic aerosol. *Science,* **255,** 423–430.

Chen, C.-T., 1994: Sensitivity of the simulated global climate to perturbations in low cloud microphysical properties. Ph.D. dissertation, Princeton University, 279 pp.

——, and V. Ramaswamy, 1995: Parameterization of the solar radiative characteristics of low clouds and studies with a general circulation model. *J. Geophys. Res.,* **100,** 11 611–11 622.

Coakley, J. A., Jr., R. L. Bernstein, and P. A. Durkee, 1987: Effect of ship-stack effluents on cloud reflectivity. *Science,* **237,** 1020–1022.

Crutcher, H. L., and J. M. Meserve, 1970: *Selected-Level Heights, Temperatures, and Dew Point Temperatures for the Northern Hemisphere.* Rep. NAVAIR 50-IC-52, U.S. Naval Weather Service, Washington, DC.

Feigelson, E. M., 1978: Preliminary radiation model of a cloudy atmosphere, I, Structure of clouds and solar radiation. *Beitr. Phys. Atmos.,* **51,** 203–229.

Greenwald, T. J., G. L. Stephens, T. H. Vonder Haar, and D. L. Jackson, 1993: A physical retrieval of cloud liquid water over the global oceans using Special Sensor Microwave/Imager (SSM/I) observations. *J. Geophys. Res.,* **98,** 18 471–18 488.

Han, Q., W. B. Rossow, and A. Lacis, 1994: Near-global survey of effective droplet radii in liquid water clouds using ISCCP data. *J. Climate,* **7,** 465–497.

Hansen, J. E., A. Lacis, D. Rind, G. Russell, P. Stone, I. Fung, R. Ruedy, and J. Lerner, 1984: Climate sensitivity: Analysis of feedback mechanisms. *Climate Processes and Climate Sensitivity, Geophys. Monogr. Ser.,* 29, Amer. Geophys. Union, 130–163.

Hartmann, D. L., M. E. Ockert-Bell, and M. L. Michelsen, 1992: The effect of cloud type on earth's energy balance: Global analysis. *J. Climate,* **5,** 1281–1304.

Held, I. M., 1993: Large-scale dynamics and global warming. *Bull. Amer. Meteor. Soc.,* **74,** 228–241.

Hoppel, W. A., J. E. Dinger, and R. E. Ruskin, 1973: Vertical profiles of CCN at various geographical location. *J. Atmos. Sci.,* **30,** 1410–1420.

Manabe, S., and R. T. Wetherald, 1967: Thermal equilibrium of the atmosphere with a given distribution of relative humidity. *J. Atmos. Sci.,* **24,** 241–259.

——, and ——, 1975: The effects of doubling the CO_2 concentration on the climate of a general circulation model. *J. Atmos. Sci.,* **32,** 3–15.

——, and R. J. Stouffer, 1980: Sensitivity of a global climate model to an increase of CO_2 concentration in the atmosphere. *J. Geophys. Res.,* **85,** 5529–5554.

——, and A. J. Broccoli, 1985: A comparison of climate model sensitivity with data from the last glacial maximum. *J. Atmos. Sci.,* **42,** 2643–2651.

——, D. G. Hahn, and J. L. Holloway, 1979: *Climate Simulation with GFDL Spectral Models of the Atmosphere.* W. L. Gates, Ed., GARP Publ. Ser. 22, WMO, 41–94.

——, R. J. Stouffer, M. J. Spelman, and K. Bryan, 1991: Transient response of a coupled ocean–atmosphere model to gradual changes of atmospheric CO_2. Part I: Annual mean response. *J. Climate,* **4,** 785–818.

Mason, B. J., 1971: *The Physics of Clouds.* Clarendon Press, 672 pp.

Mitchell, J. F. B., C. A. Wilson, and W. M. Cunnington, 1987: On CO_2 climate sensitivity and model dependence of result. *Quart. J. Roy. Meteor. Soc.,* **113,** 293–322.

Nakajima, T., and M. D. King, 1990: Determination of the optical thickness and effective particle radius of clouds from reflected solar radiation measurements. Part I: Theory. *J. Atmos. Sci.,* **47,** 1878–1893.

——, ——, J. D. Spinhirne, and L. F. Radke, 1991: Determination of the optical thickness and effective particle radius of clouds from reflected solar radiation measurements. Part II: Marine stratocumulus oservations. *J. Atmos. Sci.,* **48,** 728–750.

Peixoto, J. P., and A. H. Oort, 1992: *Physics of Climate.* Amer. Inst. Phys., 520 pp.

Radke, L. F., J. A. Coakley Jr., and M. D. King, 1989: Direct and remote sensing observation of the effect of ships on clouds. *Science,* **246,** 1146–1149.

Ramaswamy, V., and C.-T. Chen, 1993: An investigation of the global solar radiative forcing due to changes in the cloud liquid water path. *J. Geophys. Res.,* **98,** 16 703–16 712.

Roeckner, E., U. Schlese, J. Biercamp, and P. Loewe, 1987: Cloud optical depth feedbacks and climate modeling. *Nature,* **329,** 138–140.

Rossow, W. B., and A. A. Lacis, 1990: Global, seasonal cloud variations from satellite radiance measurements. Part II: Cloud properties and radiative effects. *J. Climate,* **3,** 1204–1253.

——, and R. A. Schiffer, 1991: ISCCP cloud data products. *Bull. Amer. Meteor. Soc.,* **72,** 2–20.

——, L. C. Garder, and A. A. Lacis, 1989: Global, seasonal cloud variations from satellite radiance measurements. Part I: Sensitivity of analysis. *J. Climate,* **2,** 419–458.

Schlesinger, M. E., 1988: Quantitative analysis of feedbacks in climate model simulations of CO_2-induced warming. *Physically-Based Modelling and Simulation of Climate and Climatic Change,* M. E. Schlesinger, Ed., NATO ASI Ser., Vol. 243, Reidel, 653–736.

——, 1989: Model projections of the climatic changes by increased atmospheric changes induced by increased atmospheric CO_2. *Climate and Geo-Sciences: A Challenge for Science and Society in the 21st Century,* A. Berger, S. H. Schneider, and J. Duplessy, Eds., Kluwer Academic, 375–415.

Slingo, A., 1989: A GCM parameterization for the shortwave radiative properties of water clouds. *J. Atmos. Sci.,* **46,** 1419–1427.

Somerville, R. C. J., and L. A. Remer, 1984: Cloud optical thickness feedbacks in the CO_2 climate problem. *J. Geophys. Res.,* **89,** 9668–9672.

Spelman, M. J., and S. Manabe, 1984: Influence of oceanic heat transport upon the sensitivity of a model climate. *J. Geophys. Res.,* **89,** 571–586.

Stephens, G. L., 1979: Optical properties of eight water cloud types. Division of Atmospheric Physics Tech. Paper No. 36, Commonwealth Scientific and Industrial Research Organisation, Aspendale, Australia, 35 pp.

Taljaard, J. J., H van Loon, L. Crutcher and R. L. Jenne, 1969: *Climate of the Upper Air: Southern Hemisphere,* Vol. 1. *Temperatures, Dew Points and Heights at Selected Pressure Levels.* Rep. NAVAIR 50-IC-55, U.S. Naval Weather Service, Washington, DC, 135 pp. [Available from Chief, Naval Operations.]

Tselioudis, G., W. B. Rossow, and D. Rind, 1992: Global patterns of cloud optical thickness variation with temperature. *J. Climate,* **5,** 1484–1495.

Twomey, S., M. Piepgrass, and T. L. Wolfe, 1984: An assessment of the impact of pollution on global cloud albedo. *Tellus,* **36B,** 356–366.

Untersteiner, N., 1984: The cryosphere. *The Global Climate,* J. T. Houghton, Ed., Cambridge University Press, 121–140.

Warren, S. G., C. J. Hahn, J. London, R. M. Chervin, and R. L. Jenne, 1988: Global distribution of total cloud cover and cloud type amounts over ocean. NCAR Tech. Note NCAR/TN-317+STR, National Center for Atmospheric Research, Boulder, CO, 42 pp. plus 170 maps.

Wetherald, R. T., and S. Manabe, 1975: The effects of changing the solar constant on the climate of a general circulation model. *J. Atmos. Sci.,* **32,** 2044–2059.

——, and ——, 1988: Cloud feedback processes in a general circulation model. *J. Atmos. Sci.,* **45,** 1397–1415.